

Three-Mode Variable-Frequency ZVS Modulation for Four-Switch Buck+Boost Converters With Ultra-high Efficiency

Yu, Guangyao; Dong, Jianning; Soeiro, Thiago Batista; Zhu, Gangwei; Yao, Yu; Bauer, Pavol

DOI

[10.1109/TPEL.2022.3231969](https://doi.org/10.1109/TPEL.2022.3231969)

Publication date

2022

Document Version

Final published version

Published in

IEEE Transactions on Power Electronics

Citation (APA)

Yu, G., Dong, J., Soeiro, T. B., Zhu, G., Yao, Y., & Bauer, P. (2022). Three-Mode Variable-Frequency ZVS Modulation for Four-Switch Buck+Boost Converters With Ultra-high Efficiency. *IEEE Transactions on Power Electronics*, 38(4), 4805-4819. <https://doi.org/10.1109/TPEL.2022.3231969>

Important note

To cite this publication, please use the final published version (if applicable). Please check the document version above.

Copyright

Other than for strictly personal use, it is not permitted to download, forward or distribute the text or part of it, without the consent of the author(s) and/or copyright holder(s), unless the work is under an open content license such as Creative Commons.

Takedown policy

Please contact us and provide details if you believe this document breaches copyrights. We will remove access to the work immediately and investigate your claim.

Green Open Access added to TU Delft Institutional Repository

'You share, we take care!' - Taverne project

<https://www.openaccess.nl/en/you-share-we-take-care>

Otherwise as indicated in the copyright section: the publisher is the copyright holder of this work and the author uses the Dutch legislation to make this work public.

Three-Mode Variable-Frequency ZVS Modulation for Four-Switch Buck+Boost Converters With Ultra-High Efficiency

Guangyao Yu ¹, Student Member, IEEE, Jianning Dong ¹, Senior Member, IEEE, Thiago Batista Soeiro, Senior Member, IEEE, Gangwei Zhu ¹, Student Member, IEEE, Yu Yao ¹, Student Member, IEEE, and Pavol Bauer ¹, Senior Member, IEEE

Abstract—This article introduces a three-mode variable-frequency zero-voltage switching (ZVS) modulation method for the four-switch buck+boost converter. This method makes this circuit concept well suited for applications, such as wireless power charging of electric vehicles, where this circuit operates as a power buffer between the resonant converter and the battery with the function to implement the required charging profile. Herein, the buck+boost converter operation is subdivided into three operating regions according to the converter static voltage gain, i.e., buck-, buck-boost- and boost-type modes. A ZVS turn-ON triangular current mode (TCM) control is adopted for buck-type and boost-type modes. In the buck-boost-type mode when the input-to-output voltage gain is close to unit, all the possible modulation cases are studied thoroughly based on the phase shift of the two half bridges in a full switching period. The selection of the most suitable modulation scheme is performed to minimize the rms value of the inductor current while taking into account the simplification of the practical implementation. Closed-form equations are derived, which makes it easy to implement in practice. The proposed strategy is described, analyzed, and finally verified through a 3 kW surface mounted device (SMD) silicon carbide (SiC) MOSFET-based laboratory prototype with designed input voltage of 300–600 V and the typical output voltage of 400 V class battery. The efficiency from the measured results is remarkably high, i.e., between 99.2% and 99.6% in a power range from 1 to 3 kW. Finally, tests for the operating mode transitions demonstrated the feasibility of the proposed modulation method. The power density of this converter is 4.86 kW/L.

Index Terms—DC–DC power converters, modeling, modulation, phase shift, variable frequency, zero-voltage switching (ZVS).

Manuscript received 26 August 2022; revised 16 November 2022; accepted 15 December 2022. Date of publication 26 December 2022; date of current version 14 February 2023. Recommended for publication by Associate Editor Herbert Ho-Ching Iu. (Corresponding author: Guangyao Yu.) Recommended for publication by Associate Editor H. H.-C. Iu.

Guangyao Yu, Jianning Dong, Gangwei Zhu, and Pavol Bauer are with the Faculty of Electrical Engineering, Mathematics and Computer Science, Delft University of Technology, 2628 CD Delft, Netherlands (e-mail: G.Yu-1@tudelft.nl; j.dong-4@tudelft.nl; g.zhu-2@tudelft.nl; p.bauer@tudelft.nl).

Thiago Batista Soeiro is with the Faculty of Electrical Engineering, Mathematics and Computer Science, University of Twente, 7522 NB Enschede, Netherlands (e-mail: t.batistasoeiro@utwente.nl).

Yu Yao is with the Electrical Engineering, Southeast University—Sipailou Campus, Nanjing 210096, China (e-mail: yuyao@seu.edu.cn).

Color versions of one or more figures in this article are available at <https://doi.org/10.1109/TPEL.2022.3231969>.

Digital Object Identifier 10.1109/TPEL.2022.3231969

I. INTRODUCTION

BATTERY energy storage systems (BESSs) play a vital role in the energy transition market [1], [2]. The advent of more electric transportation is strongly reliant on the BESS technology [3]. The development and performance of a BESS is dependent on the features of the dedicated power electronics-based charger/discharger regulator [4].

Today, an advantageous compound circuit for the BESS charging application is the nonisolated dc–dc converter assembled with the four-switch buck+boost converter. This circuit has both voltage step-up (boost) and voltage step-down (buck) functions. In fact, this converter has found a good fit for the application in the field of wireless power transfer (WPT) electric vehicle (EV) charging as illustrated by Fig. 1. The reasons behind the adoption of a buck+boost converter in a WPT EV charging system will be briefly discussed in the followings.

The WPT-based EV chargers usually adopt series–series (SS) compensation in the resonant dc–dc converter stage [5]. In order to achieve the highest efficiency, the equivalent dc load seen by the resonant converter $R_L = \frac{V_1}{I_1}$ (cf. Fig. 1) should match the so-called optimal load R_{opt} [6], [7], which is

$$R_{opt} = \frac{\pi^2}{8} \sqrt{R_2^2 + \omega_0^2 M^2} \frac{R_2}{R_1}. \quad (1)$$

In (1), M is the coil mutual inductance; R_1 and R_2 are the lump equivalent resistances modeling the power losses across the primary and secondary side components; ω_0 is the converter's resonant frequency. In essence, the function of the nonisolated dc–dc converter is to act as a load impedance matching converter [8], [9]. Since the optimal load depends on the mutual inductance, its condition varies with the coils' alignment. Besides, with the change of charging power, it can be imagined that the input voltage of the back-end dc–dc converter V_1 will vary in a wide range. In order to match the EV battery charging profile while allowing the switching frequency of the SS compensated resonant converter to be narrow according to the specified standards (e.g., the SAE J2954 [10]), a converter with both voltage step-up and step-down functions is, therefore, advantageous.

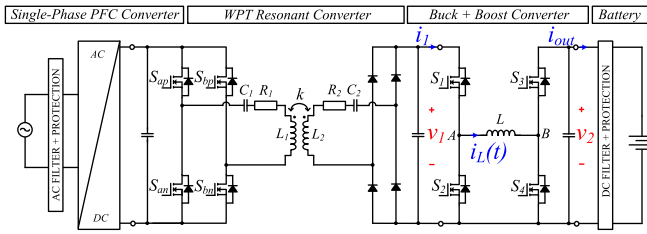


Fig. 1. SS compensated WPT system with a four-switch buck+boost converter as a back-end DC–DC converter.

The modulation strategies of the four-switch buck+boost converter can be mainly divided into the following three categories: single mode, two-mode, and three-mode operations. Under each category, either hard-switched or soft-switched modulation control could be applied. Single-mode operation is the simplest control method when buck-boost-type mode is adopted [11], i.e., switches S_1 and S_4 (cf. Fig. 1) turn on and off simultaneously, which operates exactly the same as a single-switch buck–boost converter but with a noninverting output voltage. However, this modulation scheme usually results in poor efficiency due to the high switching and conduction losses. To address this problem, two-mode operation was introduced [12], [13], [14], [15], [16]. In two-mode operation, buck-type or boost-type mode is adopted based on the input and output voltages. There are several advantages of this operation: First, only two switches are active, so the switching losses could be reduced; Second, the conduction losses could also be lower; Third, with adoption of zero-voltage switching (ZVS) turn-ON triangular current mode (TCM) control [17], [18], [19], [20], the efficiency of SiC MOSFET-based buck or boost converters can be higher than 99%. However, due to the duty cycle limitation in practice, there will be a voltage transition zone that cannot be covered by the two-mode operation, which is the main drawback of this control strategy. Hence, three-mode operation was introduced [21], [22], [23], [24], with an added zone between the buck-type and boost-type modes, the output voltage can be regulated well in this zone. Two-edge modulation was proposed in [22] and [25] to reduce the conduction losses, i.e., switches S_1 and S_4 are trailing-edge and leading-edge modulated resulting in a lower current rms value, however, it is still a hard-switched modulation [22], [24], [25]. With such a concept, the highest power efficiency was 97.8% at rated power of 300 W [22] and 98.5% at 250 W [25].

Although hard-switched SiC MOSFET-based dc–dc converter could also possibly achieve power efficiency higher than 99% [26], [27], the high rate of voltage change (dV/dt) due to the shorter switching transients will cause increased electromagnetic interference emissions [28]. Furthermore, with the increasing requirements for power density and efficiency, ultra-high-frequency converters can only be built through soft-switching techniques to achieve acceptable power efficiency [21], [29]. Considerable efforts have been made to implement the ZVS control for the buck+boost converters in recent years. In [21] and [23], the TCM-ZVS control was extended to the buck-boost-type mode, however, the operation in this mode was not optimized, and thus, a sudden efficiency drop was observed. The reported conversion efficiency was between 98% and 98.5% for

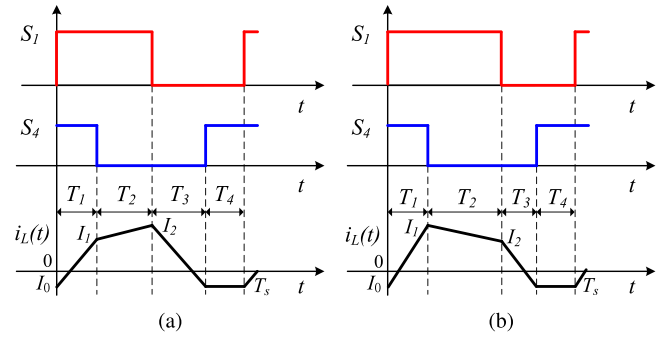


Fig. 2. Fixed-frequency four-segment inductor current ZVS control method, I_0 is negative. (a) $V_1 > V_2$. (b) $V_1 < V_2$.

a 2.5 kW prototype by Yu et al. [23]. Yu et al. [30] and [31] further optimized this ZVS control. In [30], the assumption of an equal duty cycle was applied to both switches S_1 and S_4 , and the highest efficiency was 99.4% for a 3 kW prototype. However, both the detailed mathematical analysis and practical implementation steps are missing in [30] and [31]. In [32], an improved control strategy was proposed for the intermediate mode of variable-frequency modulation, however, the rms value of the inductor current was not studied and an evident efficiency drop was still observed in the intermediate mode with a value around 4%. The reported efficiency was between 93% and 96.9% for a 300 W prototype.

Apart from variable-frequency ZVS modulation, fixed-frequency four-segment inductor current ZVS control were proposed and studied [28], [33], [34], [35], [36], [37]. In order to make descriptions clearer, the concept is illustrated in Fig. 2. In [33], the general descriptions of this modulation concept were given, but without detailed mathematical analysis. With the same control concept, Waffler et al. [28] studied the switching times of the switches in a period to maximize the transferred power under ZVS conditions, but the optimization to further minimize inductor current rms value was missing, and the peak efficiency was 98.3% for a 12 kW prototype with a power density of 17.4 kW/L. Theoretical analysis for the current rms value minimization was presented in [34], however, due to the complexity of the equations, the optimized switching times can only be calculated offline. Nevertheless, the switching frequency at 800 kHz was impressive and the peak efficiency was 98% for a 300 W prototype. Based on the research work of [34], Tian et al. further found a monotonic relationship between the rms and peak value of the inductor current through plotting, however, with the assumption of letting the corner current [I_1 in Fig. 2(a), I_2 in Fig. 2(b)] equal to the ZVS turn-ON current, the analytical expressions for the switching times can actually be determined, which were not given in [35]. By further checking the proposed method in [35], a combination control of fixed- and variable-frequency modulations is adopted, which increases the control complexity. In [36], it was found that through selecting a certain T_1 (cf. Fig. 2), the conduction losses and the core losses could be minimized, however, the value of T_1 depends on the working conditions and a look-up table was needed. The peak efficiency was 98.1% for a 280 W prototype operating at 1 MHz frequency [36]. Due to the calculation complexity of the

TABLE I
SUMMARY OF STATE-OF-THE-ART FOUR-SWITCH BUCK+BOOST CONVERTERS

References	Power	Year	Input (V)	Output (V)	Frequency (kHz)	MOSFET type	Switching type	Peak Eff. (%)	Power density (kW/L)
This article	3 kW	2022	300–600	360–400	20–160	SiC	Soft	99.6	4.86
CU-Boulder [13]	500 W	2012	12–38	21–32	100	Si HEXFET	Hard	97.0	N/A
UCF [14]	100 W	2019	11–50	12–36	80–150	Si OptiMOS	Hard	99.31	3.67
DTU [21]	100 W	2017	30–60	30–60	10 ⁴	GaN	Soft	94.4	6.25
NCAA [22]	300 W	2009	36–75	48	200 and 40	Si	Hard	97.8	N/A
Fraunhofer Institute [23]	2.5 kW	2015	400	100–550	N/A	SiC	Soft	>99.0	N/A
Sungkyunkwan University [25]	250 W	2016	15–40	0–43	200	Si OptiMOS	Hard	98.5	N/A
ETH Zurich [28]	12 kW	2009	<450	<450	100	Si HiPerFET	Soft	98.3	17.4
Fraunhofer Institute [30]	3 kW	2016	400	150–500	N/A	SiC	Soft	99.4	N/A
Zhejiang University [34]	300 W	2019	36–72	48	800	Si OptiMOS	Soft	98.0	N/A
Zhejiang University [35]	300 W	2022	36–60	36–60	700–800	Si NexFET	Soft	98.5	N/A
Southeast University [36]	280 W	2021	36–72	48	1000	GaN	Soft	98.1	N/A

four-segment current ZVS control method, a special case is to set a fixed duty cycle to S_1 or S_4 [37], then the calculations can be simplified considerably. A summary of state-of-the-art four-switch buck+boost converters is shown in Table I.

A thorough study of a three-mode variable-frequency soft-switched modulation strategy for the four-switch buck+boost converter is found to be missing in the literature. The main purpose and contribution of this article is to analyze each possible modulation case in the buck-boost-type mode through the phase shift between S_1 and S_4 in a full switching period with a new set of derived closed-form equations, which can be used to determine parameters, such as switching frequency and inductor current rms value. The closed-form equations of the inductor current rms value are usually missing in the literature due to the complicated calculations, thus, the optimization of the peak current [38] was usually adopted rather than the rms value. In this work, it is found that in the buck-boost-type mode, the three-segment inductor current ZVS modulation is the most suitable scheme because it greatly simplifies the converter operation while maintaining a high-efficiency performance. The proposed modulation strategy combines advantages from different operating modes, thus, the converter can always operate efficiently in a wide range. Besides, the mode transition tests were also provided to demonstrate the feasibility of the proposed modulation method.

The rest of this article is organized as follows. Section II presents the working principle of the four-switch buck+boost converter, the proposed modulation strategy featuring ZVS turn-on, and finally the derived formulae. In Section III, design considerations including the selection of the switched ZVS current and inductance are shown. In Section IV, the studied modulation is evaluated through a 3 kW surface mounted device (SMD) silicon carbide (SiC) MOSFET-based prototype. Finally, Section V concludes this article.

II. WORKING PRINCIPLE OF THE MODULATION STRATEGY

A. Voltage Gain of the Four-Switch Buck+Boost Converter

The four-switch buck+boost converter is composed of two half-bridge circuits, as shown in Fig. 1. S_1 and S_2 form the buck-type conversion while S_3 and S_4 form the boost-type conversion. The pulse width modulation (PWM) signals applied to each bridge are complementary.

Some assumptions are made for the following analysis. First, the dead-time influence is neglected in this section; Second, the inductor has a constant value; Third, the input and output voltages are taken as constant dc values.

Defining d_1 and d_2 as the duty cycles of S_1 and S_4 , respectively. Based on the volt-second balance of the inductor under steady state, the average voltage across points A and B shown in Fig. 1 should be zero. The average voltages of points A and B with respect to the bottom-side dc-bus rail are

$$\bar{v}_A = d_1 V_1 \quad (2)$$

$$\bar{v}_B = (1 - d_2) V_2. \quad (3)$$

Therefore, $\bar{v}_A = \bar{v}_B$ leads to the voltage gain equation as follows:

$$G_v = \frac{V_2}{V_1} = \frac{d_1}{1 - d_2}. \quad (4)$$

Equation (4) always holds regardless of the power level. Based on (4), infinite control schemes can be found to realize a certain voltage gain since d_1 and d_2 can be controlled independently.

B. Soft Switching Under Buck-Boost-Type Mode With Possible Modulations

Depending on the minimum pulsewidth and switching frequency, the minimum and maximum duty cycle of the PWM signals can be different [24]. In this article, the maximum and minimum duty cycles are set as 0.9 and 0.1, then, the maximum gain under buck mode is 0.9 and the minimum gain under boost mode is 1.11. So, the voltage gain under buck-boost-type mode needs to cover the voltage gain between these two values. Based on (4), the difference between d_1 and d_2 is

$$\Delta d = d_1 - d_2 = d_1 \left(1 + \frac{1}{G_v} \right) - 1. \quad (5)$$

If $\Delta d > 0$, as will be seen later, the modulation analysis will be simpler since for each step-down or step-up case, only four modulation types need to be analyzed. When $\Delta d > 0$, (6) can be derived as

$$d_1 > \frac{1}{1 + \frac{1}{G_v}}. \quad (6)$$

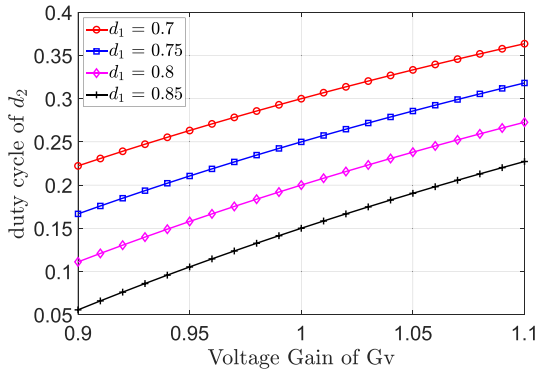


Fig. 3. Duty cycle of d_2 in terms of different d_1 . d_2 is always smaller than d_1 .

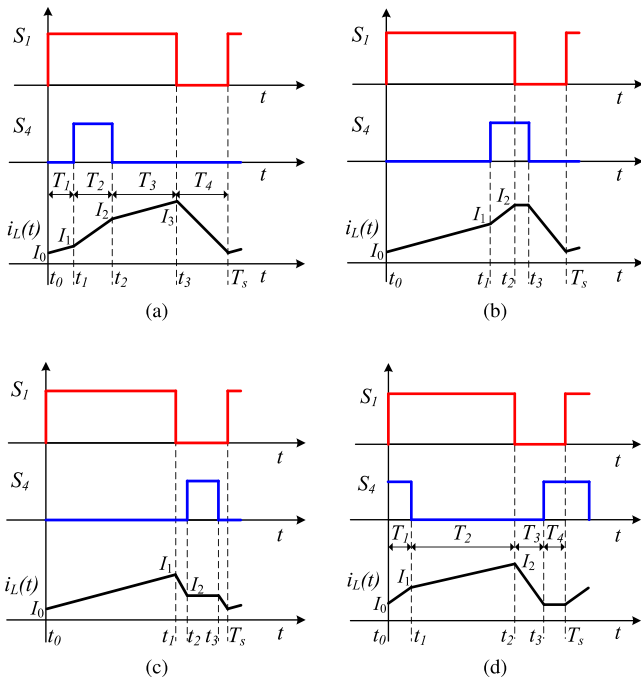


Fig. 4. All four possible modulation cases when $V_1 > V_2$ under buck-boost-type mode.

Substitute $G_v = 1.11$ into (6), then when $d_1 > 0.526$, d_1 is always larger than d_2 . Fig. 3 shows the duty cycle of d_2 with different values of d_1 .

For the rest analysis in this section, $d_1 > d_2$ always holds.

To fully analyze each possible modulation case, the phase shift between the PWM signals of S_1 and S_4 has to be carried out in a full switching period.

1) When $V_1 > V_2$: From (4), one has

$$d_1 + d_2 < 1. \quad (7)$$

Fig. 4 shows all four possible modulation cases when $V_1 > V_2$. It should be noted that the modulations with boundary overlapping are not drawn since they are special cases.

In order to turn on the switches under ZVS condition, the switched current during the dead time needs to first freewheel

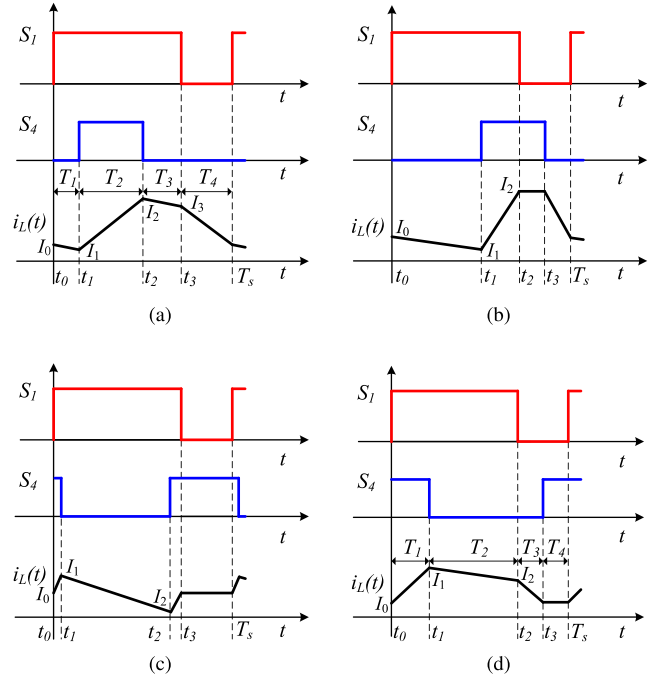


Fig. 5. All four possible modulation cases when $V_1 < V_2$ under buck-boost-type mode.

through the MOSFET body diode, then the MOSFET to be switched can be turned on at zero drain–source voltage due to the low forward voltage drop of the body diode. So, the ZVS turn-ON in a four-switch buck+boost converter requires the inductor current to be negative during the switching-ON transition for S_1 and S_4 , and to be positive while turning on S_2 and S_3 .

The requirements for the four switches to realize soft switching with the modulation cases shown in Fig. 4 are: for Fig. 4(a), $I_1 < 0$ and $I_2 > 0$; for Fig. 4(b), $I_1 < 0$; for Fig. 4(d), $I_0 < 0$ and $I_1 > 0$. However, for Fig. 4(c), it is impossible to realize ZVS for all the switches since I_2 has to be positive (ZVS turn-ON of S_3) and negative (ZVS turn-ON of S_4) simultaneously.

When considering the modulation case given in Fig. 4(b), it is not a good choice since both I_0 and I_1 are negative, thus, I_2 should be positive to transfer power from the input to output side and the value of I_2 could be considerably large, which could bring high current stresses to other components. Therefore, only the modulation cases in Fig. 4(a) and (d) will be considered in this article.

2) When $V_1 < V_2$: From (4), one has

$$d_1 + d_2 > 1. \quad (8)$$

Fig. 5 shows all four possible modulation cases when $V_1 < V_2$.

Based on the ZVS conditions mentioned earlier, the requirements for the four switches to achieve soft switching in Fig. 5 are: for Fig. 5(a), $I_0 < 0$ and $I_3 > 0$; for Fig. 5(b), $I_0 < 0$; for Fig. 5(d), $I_0 < 0$ and $I_2 > 0$. Similar to the case of Fig. 4(c), for Fig. 5(c), it is also impossible to realize ZVS for all the switches. The modulation of Fig. 5(b) also suffers from high peak current

of I_2 . Therefore, the modulation cases in Fig. 5(a) and (d) will be considered.

C. RMS Value of the Inductor Current With Phase Shift

This section gives the closed-form analytical equations of the inductor current rms value under ZVS conditions. In fact, this value also determines the conduction losses of the MOSFETS, since

$$I_{\text{rms}_S1}^2 + I_{\text{rms}_S2}^2 = I_{\text{rms}_S3}^2 + I_{\text{rms}_S4}^2 = I_{\text{rms}_L}^2. \quad (9)$$

I_{rms_S1} – I_{rms_S4} are the current rms values through channels of S_1 – S_4 , and I_{rms_L} is the inductor current rms value.

1) When $V_1 > V_2$: I_1 for the modulation case in Fig. 4(a) and I_0 in Fig. 4(d) are selected as a fixed negative value for the variable-frequency ZVS modulation.

In Fig. 4(a)

$$T_1 + T_2 + T_3 + T_4 = T_s. \quad (10)$$

T_1 is defined as $T_1 = \alpha T_s$, α is the phase shift between S_1 and S_4 . Therefore, T_2 , T_3 , and T_4 are

$$T_2 = d_2 T_s, T_3 = (d_1 - d_2 - \alpha) T_s, T_4 = (1 - d_1) T_s. \quad (11)$$

The inductor current in a switching period is given below with $t_0 = 0$

$$i_L(t) = \begin{cases} I_0 + \frac{V_1 - V_2}{L} t, 0 < t \leq t_1 \\ i_L(t_1) + \frac{V_1}{L}(t - t_1), t_1 < t \leq t_2 \\ i_L(t_2) + \frac{V_1 - V_2}{L}(t - t_2), t_2 < t \leq t_3 \\ i_L(t_3) - \frac{V_2}{L}(t - t_3), t_3 < t \leq T_s. \end{cases} \quad (12)$$

According to (12), express I_0 , I_2 , and I_3 by I_1 , one can obtain

$$\begin{cases} I_0 = I_1 - \frac{V_1 - V_2}{L} \alpha T_s \\ I_2 = I_1 + \frac{V_1}{L} d_2 T_s \\ I_3 = I_1 + \frac{V_1 - V_2}{L} (d_1 - \alpha) T_s + \frac{V_2}{L} d_2 T_s. \end{cases} \quad (13)$$

Since the power is only transferred when S_3 is on, so, the average output current is

$$I_{\text{out}} = \frac{I_0 + I_1}{2} \alpha + \frac{I_2 + I_3}{2} (d_1 - d_2 - \alpha) + \frac{I_3 + I_0}{2} (1 - d_1), \quad (14)$$

based on (4), (13), (14), after simplification, (15) can be derived as

$$L f_s = \frac{\frac{V_1}{2} [d_1(1 - d_1) + d_2(d_1 - d_2) - 2\alpha(1 - d_1)]}{I_{\text{out}} - I_1(1 - d_2)}. \quad (15)$$

f_s is the switching frequency. According to (A3) derived in the Appendix showing the rms value calculation of a general polyline function, the rms value of the inductor current is

$$I_{\text{rms}_L} = \sqrt{\alpha \frac{I_0^2 + I_1^2 + I_0 I_1}{3} + d_2 \frac{I_1^2 + I_2^2 + I_1 I_2}{3} + (d_1 - d_2 - \alpha) \frac{I_2^2 + I_3^2 + I_2 I_3}{3} + (1 - d_1) \frac{I_0^2 + I_3^2 + I_0 I_3}{3}}. \quad (16)$$

According to Fig. 4(a) and (15), α should satisfy

$$0 \leq \alpha < \min \left\{ d_1 - d_2, \frac{d_1(1 - d_1) + d_2(d_1 - d_2)}{2(1 - d_1)} \right\}. \quad (17)$$

For the case in Fig. 4(d), the phase shift between S_1 and S_4 is defined by T_4 , which is $T_4 = -\beta T_s$ and β is defined as a negative value. So, T_1 , T_2 , and T_3 are

$$T_1 = (d_2 + \beta) T_s, T_2 = (d_1 - d_2 - \beta) T_s, T_3 = (1 - d_1 + \beta) T_s. \quad (18)$$

The inductor current in a switching period is

$$i_L(t) = \begin{cases} I_0 + \frac{V_1}{L} t, 0 < t \leq t_1 \\ i_L(t_1) + \frac{V_1 - V_2}{L}(t - t_1), t_1 < t \leq t_2 \\ i_L(t_2) - \frac{V_2}{L}(t - t_2), t_2 < t \leq t_3 \\ I_0, t_3 < t \leq T_s. \end{cases} \quad (19)$$

According to (19) and by relating the values of I_1 and I_2 to I_0 , one can derive

$$\begin{cases} I_1 = I_0 + \frac{V_1}{L} (d_2 + \beta) T_s \\ I_2 = I_0 + \frac{V_1}{L} d_1 T_s - \frac{V_2}{L} (d_1 - d_2 - \beta) T_s. \end{cases} \quad (20)$$

The average output current is

$$I_{\text{out}} = \frac{I_1 + I_2}{2} (d_1 - d_2 - \beta) + \frac{I_2 + I_0}{2} (1 - d_1 + \beta). \quad (21)$$

After simplification, (22) can be derived as

$$L f_s = \frac{\frac{V_1}{2} [d_1(1 - d_1) + d_2(d_1 - d_2) + \beta(2d_1 - 2d_2 - \beta)]}{I_{\text{out}} - I_0(1 - d_2)}. \quad (22)$$

Similar to (16), the inductor current rms value can also be derived, which is

$$I_{\text{rms}_L} = \sqrt{(d_2 + \beta) \frac{I_0^2 + I_1^2 + I_0 I_1}{3} + (d_1 - d_2 - \beta) \frac{I_1^2 + I_2^2 + I_1 I_2}{3} + (1 - d_1 + \beta) \frac{I_2^2 + I_0^2 + I_2 I_0}{3} + (-\beta) I_0^2}. \quad (23)$$

According to Fig. 4(d) and (22), the phase shift of β should satisfy: $-d_2 < \beta \leq 0$.

2) When $V_1 < V_2$: Both the current values of I_0 in Fig. 5(a) and (d) are set as a fixed negative value for variable-frequency ZVS modulation.

For the case of Fig. 5(a), the expression of the inductor current in a switching period is the same as (12) and by linking the values of I_1 , I_2 and I_3 to I_0 , one can obtain

$$\begin{cases} I_1 = I_0 + \frac{V_1 - V_2}{L} \alpha T_s \\ I_2 = I_0 + \frac{V_1}{L} (\alpha + d_2) T_s - \frac{V_2}{L} \alpha T_s \\ I_3 = I_0 + \frac{V_2}{L} (1 - d_1) T_s. \end{cases} \quad (24)$$

The expression of I_{out} is the same as (14), therefore, (25) can be obtained as

$$L f_s = \frac{\frac{V_1}{2} [d_1(1 - d_1) + d_2(d_1 - d_2) - 2\alpha d_2]}{I_{\text{out}} - I_0(1 - d_2)}. \quad (25)$$

According to Fig. 5(a) and (25), α should satisfy

$$0 \leq \alpha < \min \left\{ d_1 - d_2, \frac{d_1(1 - d_1) + d_2(d_1 - d_2)}{2d_2} \right\}. \quad (26)$$

For the modulation case of Fig. 5(d), the same formula of (22) can be obtained with $d_1 - 1 < \beta \leq 0$.

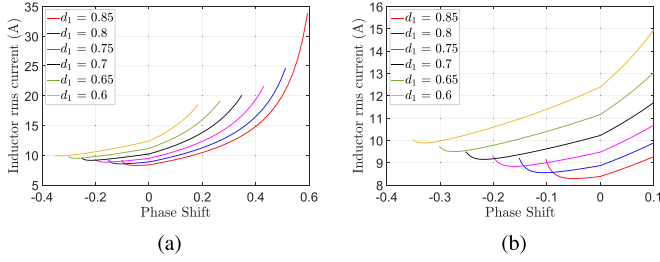


Fig. 6. Inductor rms current at different values of d_1 , $V_1 = 420$ V, $V_2 = 400$ V, $P_o = 3$ kW, ZVS current is -2 A. Phase-shift range is limited by ZVS. (b) is a partial enlargement of (a).

The inductor current rms value can then be calculated accordingly for both cases and it is skipped here.

3) *When $V_1 = V_2$:* This is the boundary case between $V_1 > V_2$ and $V_1 < V_2$. By comparing (15) and (25), when $V_1 = V_2$, one has $d_1 + d_2 = 1$ and $I_0 = I_1$, so, the calculated result of Lf_s is the same from these two equations.

4) *Independence Between Inductance and Inductor Current RMS Value:* For variable-frequency ZVS modulation, the rms value of the inductor current is independent of its inductance if the frequency is not limited. To prove this, take the case in Fig. 4(a) as an example, substitute the switching frequency derived from (15) into (13), then

$$I_0 = I_1 - \frac{(V_1 - V_2)\alpha}{k}, I_2 = I_1 + \frac{V_1 d_2}{k} \quad (27)$$

$$I_3 = I_1 + \frac{(V_1 - V_2)(d_1 - \alpha)}{k} + \frac{V_2 d_2}{k}.$$

In (27), $k = \frac{V_1}{2} [d_1(1-d_1) + d_2(d_1-d_2) - 2\alpha(1-d_1)]$. By checking these equations, the inductor variable L is eliminated. According to the rms value expression of (16), L will not influence the inductor current rms value. Furthermore, the corner value of the inductor current also does not depend on the inductance. The proof is similar for other cases. This property makes the conclusions drawn in this article more general.

5) *Duty Cycle Influence on Inductor RMS Current:* A specific example with parameters closer to the final design will be given to show the current rms value with phase shift.

The selected parameters are: The power of P_o is selected at two values of 3 kW and 1 kW, V_2 is 400 V, ZVS current is set to -2 A, as an example, i.e., $I_1 = -2$ A for Fig. 4(a), $I_0 = -2$ A for Fig. 4(d), Fig. 5(a) and (d), duty cycle of d_1 varies from 0.6 to 0.85.

According to the previous derived equations for inductor rms current calculation, the results of this example are shown in Figs. 6–9. The phase-shift range is restricted by ZVS.

From Figs. 6 to 9, it can be seen that the inductor current rms value increases as α increases. Generally, a larger value of d_1 is beneficial in terms of conduction loss reduction due to a smaller rms value of the inductor current. With a larger value selection of d_1 , the negative phase-shift range for ZVS is also smaller. Although the optimum phase shift in terms of minimum current rms value is not zero, the difference between the minimum rms value and the one at zero phase shift is negligible when d_1 is selected to be a larger enough and reasonable value, e.g., 0.8.

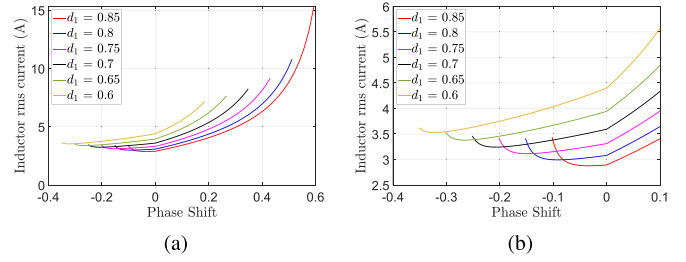


Fig. 7. Inductor rms current at different values of d_1 , $V_1 = 420$ V, $V_2 = 400$ V, $P_o = 1$ kW, ZVS current is -2 A. Phase-shift range is limited by ZVS. (b) is a partial enlargement of (a).

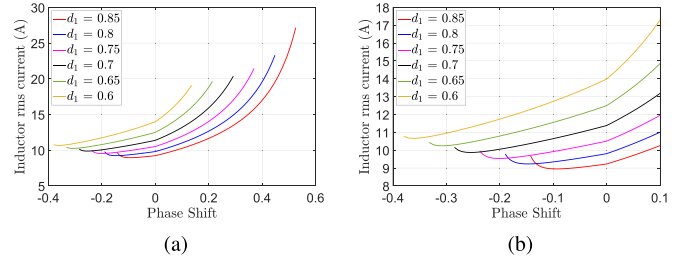


Fig. 8. Inductor rms current at different values of d_1 , $V_1 = 380$ V, $V_2 = 400$ V, $P_o = 3$ kW, ZVS current is -2 A. Phase-shift range is limited by ZVS. (b) is a partial enlargement of (a).

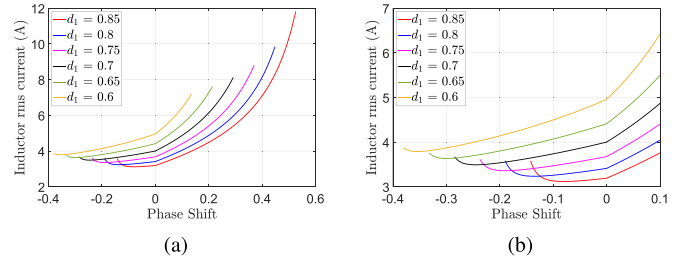


Fig. 9. Inductor rms current at different values of d_1 , $V_1 = 380$ V, $V_2 = 400$ V, $P_o = 1$ kW, ZVS current is -2 A. Phase-shift range is limited by ZVS. (b) is a partial enlargement of (a).

Therefore, to make the converter operation more convenient and robust in practice, the phase shift is selected at zero in the buck-boost-type mode, i.e., three-segment inductor current modulation is adopted.

Once this modulation is adopted, then (15), (22), and (25) can be simplified as

$$Lf_s = \frac{V_1 [d_1(1-d_1) + d_2(d_1-d_2)]}{I_{out} - I_0(1-d_2)}. \quad (28)$$

I_0 in (28) is shown in Fig. 10.

The current values of I_1 and I_2 can also be simplified as

$$I_1 = I_0 + \frac{V_1}{k} d_2, I_2 = I_0 + \frac{V_2}{k} (1-d_1). \quad (29)$$

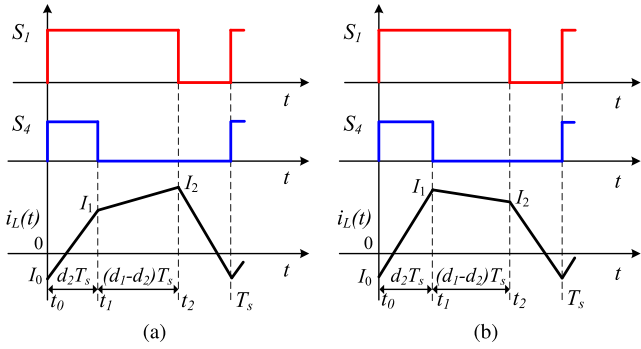


Fig. 10. Modulation in buck-boost-type mode with zero phase shift. (a) $V_1 > V_2$. (b) $V_1 < V_2$.

In (29), $k = \frac{V_1[d_1(1-d_1)+d_2(d_1-d_2)]}{I_{out}-I_0(1-d_2)}$. The inductor current rms value is

$$I_{rms_L} = \sqrt{\frac{d_2 \frac{I_0^2 + I_1^2 + I_0 I_1}{3} + (d_1 - d_2) \frac{I_1^2 + I_2^2 + I_1 I_2}{3} + (1 - d_1) \frac{I_2^2 + I_0^2 + I_2 I_0}{3}}}{3}} \quad (30)$$

6) *Duty Cycle Influence on ZVS Power Range Under Buck-Boost-Type Mode*: Different from the TCM-ZVS buck or boost-type modulation, which could have full power ZVS range, for the adopted modulation strategy in buck-boost-type mode, the current value of I_1 shown in Fig. 10(a) or I_2 in Fig. 10(b) should also satisfy the minimum ZVS current requirement. When the load decreases to a certain extent when I_1 or I_2 reduces to $-I_0$, i.e., the ZVS current, then switch S_3 or S_2 starts to lose ZVS turn-ON.

In Fig. 10(a), let $I_1 = -I_0 = I_{zvs}$, the power level when the switch S_3 starts to lose ZVS turn-ON can be expressed as

$$P_{zvs_min} = V_2 I_{zvs} \frac{(d_1 - d_2)(1 - d_1)}{d_2}. \quad (31)$$

In Fig. 10(b), let $I_2 = -I_0 = I_{zvs}$, the power level when the switch S_2 starts to lose ZVS turn-ON is

$$P_{zvs_min} = V_2 I_{zvs} \frac{d_2(1 - d_2)(d_1 - d_2)}{d_1(1 - d_1)}. \quad (32)$$

Equations (31) and (32) lead to the same result when $V_1 = V_2$ since $d_1 + d_2 = 1$. Fig. 11 shows the duty cycle influence on the value of $\frac{P_{zvs_min}}{V_2 I_{zvs}}$. As it can be seen, with a larger duty cycle of d_1 , the converter is more likely to lose ZVS of a certain switch. Due to the possible ZVS loss, the efficiency under buck-boost-type mode will drop more prominently in light load compared with the TCM-ZVS buck or boost-type modulation schemes. This can be seen by the experimental results of the efficiency curves discussed in Section IV. However, a larger value of d_1 is beneficial in terms of conduction losses, which has been discussed previously. So, in this article, combined with consideration of d_2 given in Fig. 3, d_1 will be selected at 0.8 in the transition mode.

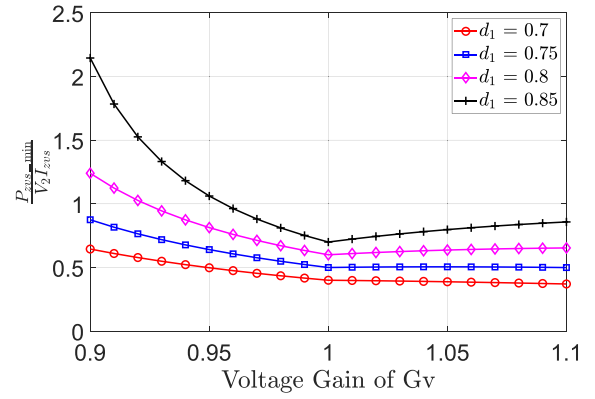


Fig. 11. Duty cycle influence on $\frac{P_{zvs_min}}{V_2 I_{zvs}}$.

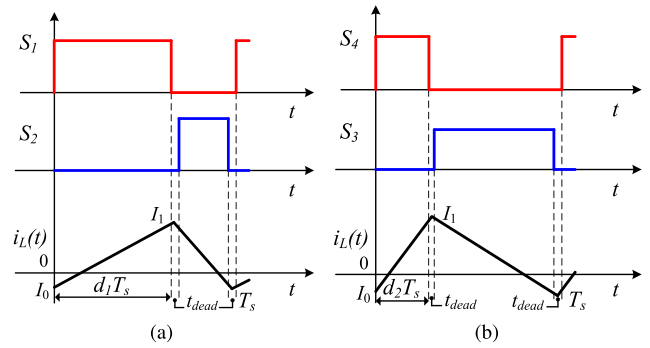


Fig. 12. TCM-ZVS inductor current waveforms and PWM signals. (a) Buck-type mode. (b) Boost-type mode.

D. TCM-ZVS Buck, Boost Operation

When the converter operates out of the transition zone, simply, only buck or boost mode could be adopted. The TCM-ZVS modulation will be briefly described as follows.

1) *TCM-ZVS Buck*: In buck-type mode, the switch S_3 is always on. The switching waveforms is given in Fig. 12(a). The equations under this mode can be written as

$$I_1 = I_0 + \frac{V_1 - V_2}{L} d_1 T_s, V_2 = d_1 V_1, I_{out} = \frac{I_0 + I_1}{2}. \quad (33)$$

I_0 and I_1 are the minimum and maximum inductor current values. After simplification, the switching frequency is derived as

$$f_s = \frac{V_1 d_1 (1 - d_1)}{2L(I_{out} - I_0)}. \quad (34)$$

2) *TCM-ZVS Boost*: In boost-type mode, the switch S_1 is always on. Fig. 12(b) shows the switching waveforms of the TCM-ZVS boost operation. The equations for this mode are

$$I_1 = I_0 + \frac{V_1}{L} d_2 T_s, V_2 = \frac{V_1}{1 - d_2}, I_{out} = \frac{I_0 + I_1}{2} (1 - d_2). \quad (35)$$

After simplification, the switching frequency is

$$f_s = \frac{V_1 d_2 (1 - d_2)}{2L[I_{out} - I_0(1 - d_2)]}. \quad (36)$$

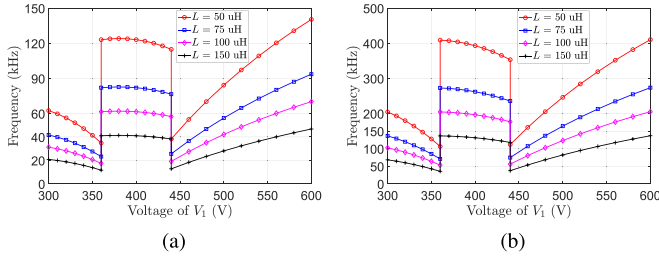


Fig. 13. Switching frequencies (without frequency restrictions) with different inductance values under three-mode modulations, $I_0 = -2$ A, $d_1 = 0.8$ in buck-boost-type mode, $V_2 = 400$ V. (a) $P_o = 3$ kW. (b) $P_o = 500$ W.

In fact, the frequency for TCM-ZVS buck or boost-type modulation can also be derived by simply applying the corresponding duty cycle values to (28). For example, substitute $d_2 = 0$ into (28), then the frequency for TCM-ZVS buck-type modulation is derived, which is the same as (34).

III. DESIGN CONSIDERATIONS

After determining the modulation scheme described in Section II, some key factors must be considered carefully including the switched current of the inductor for ensuring the ZVS turn-ON operation, the inductance value selection based on the switching frequency range, and the inductor design.

A. Inductance Value Selection

Before the inductor design, the value of the inductance needs to be determined first since this will influence the switching frequency range of the converter. In this article, the switching frequency is chosen between 20 kHz and 160 kHz based on the gate driver capability.

Since the switching frequency depends on the ZVS current, as a first step estimation described in [34] and [35], the inductor current to achieve ZVS should satisfy

$$I_{ZVS} \geq \frac{2C_{oss} \max\{V_1, V_2\}}{t_{dead}}. \quad (37)$$

I_{ZVS} is the absolute value of the instantaneous inductor current at the switching instant, C_{oss} is the lump equivalent output capacitance of the MOSFET and t_{dead} is the dead time. To build the converter prototype, each MOSFET switch was composed of three hard-paralleled SMD SiC MOSFETS of G3R75MT12 J, according to its datasheet, the voltage-related effective output capacitance is 85 pF, therefore, C_{oss} is assumed to be 255 pF. By considering the dead time value around 100 to 500 ns for SiC MOSFETS [39], the ZVS current is selected as -2 A to determine the switching frequency.

The switching frequencies under different inductance values are given in Fig. 13 with operating power at 3 kW and 500 W, respectively. As it can be seen, if there is no frequency restrictions, the frequency at light load will become relatively high, therefore, it is necessary to set a switching frequency limit.

By checking the frequency curve, one can find that there are two abrupt frequency changes at the boundary of different

TABLE II
INDUCTANCE AND EQUIVALENT RESISTANCE OF THE INDUCTOR

	20 kHz	60 kHz	100 kHz	160 kHz
L (μ H)	102.79	102.84	102.70	102.65
R_s (m Ω)	32.41	68.45	96.69	187.14

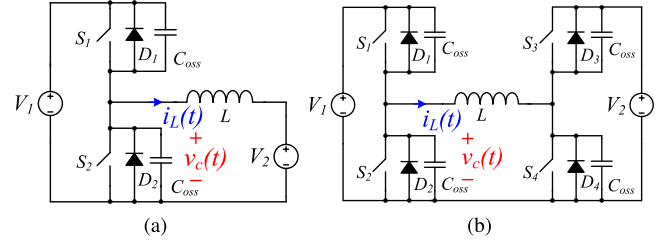


Fig. 14. Equivalent circuit during resonant interval. (a) Buck-type mode. (b) Buck-boost-type mode.

modes, i.e., the boundary between boost-type and buck-boost-type modes, and buck-boost-type and buck-type modes. In this article, the inductance of 100 μ H will be adopted.

The inductor was built using PM 74/59 core with N87 material. The inductance and the equivalent series resistance measured by Agilent 4294 A precision impedance analyzer are given in Table II at different frequencies.

B. Resonant Circuit Analysis During Dead Time

A precondition for (37) is that the inductor current is assumed to be constant during the dead time, which might not be true in some conditions, such as the cases when a longer dead time or a smaller inductance is adopted [40], [41], which could possibly bring the negative inductor current back to zero and then resonate with the output capacitors causing a loss of the desired ZVS turn-ON. Besides, a ZVS current with an unnecessary larger absolute value could also lead to a higher conduction loss due to a higher rms current. Hence, it is important and meaningful to study the resonant behavior during the dead time in a more detailed way [41].

Below, the resonant behavior under buck-type and buck-boost-type modes will be studied and compared since in buck-type mode, the input voltage can be as high as 600 V, which proposes a higher requirement to achieve ZVS than in boost-type mode.

1) *Buck-Type Mode*: The equivalent circuit during resonant interval under buck-type mode is redrawn in Fig. 14(a).

Suppose the initial inductor current at the beginning of the dead time when S_1 and S_2 are both off is $-I_{ZVS}$ (I_{ZVS} is a positive value). The drain-source voltage of S_2 ($v_c(t)$) and the inductor current ($i_L(t)$) during the resonant interval before conduction of the upper diode are

$$i_L(t) = - \left(I_{ZVS} \cos \omega_0 t + \frac{V_2}{Z_0} \sin \omega_0 t \right) \quad (38)$$

$$v_c(t) = V_2(1 - \cos \omega_0 t) + Z_0 I_{ZVS} \sin \omega_0 t, \quad (39)$$

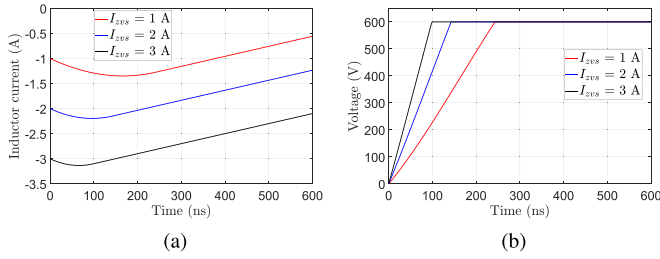


Fig. 15. $i_L(t)$ and $v_c(t)$ when $V_1 = 600$ V and $V_2 = 400$ V, $L = 100$ μ H, $C_{oss} = 255$ pF. (a) Inductor current of $i_L(t)$. (b) Voltage of $v_c(t)$.

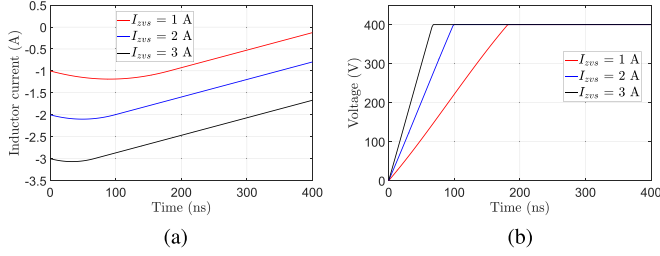


Fig. 16. $i_L(t)$ and $v_c(t)$ when $V_1 = V_2 = 400$ V, $L = 100$ μ H, $C_{oss} = 255$ pF. (a) Inductor current of $i_L(t)$. (b) Voltage of $v_c(t)$.

where $\omega_0 = \frac{1}{\sqrt{2LC_{oss}}}$, $Z_0 = \sqrt{\frac{L}{2C_{oss}}}$.

When $v_c(t)$ reaches the value of V_1 , the upper diode will conduct, and then the inductor current will decrease (the absolute value) linearly. Fig. 15 shows the curves of $v_c(t)$ and $i_L(t)$ with three different initial inductor current values at -1 A, -2 A, and -3 A.

2) *Buck-Boost-Type Mode*: The equivalent circuit during the resonant interval under buck-boost-type mode is redrawn in Fig. 14(b).

There is a slight difference in time for the drain–source voltages of S_1 and S_4 to reach zero if V_1 is not equal to V_2 , however, this time difference is relatively small and to simplify the analysis, one can assume $V_1 = V_2 = V_s$. This assumption makes sense since in buck-boost-type mode, the difference of V_1 and V_2 is relatively small. The equations of $i_L(t)$ and $v_c(t)$ during the resonant interval before the conduction of diodes are

$$i_L(t) = - \left(I_{ZVS} \cos \omega_0 t + \frac{V_s}{Z_0} \sin \omega_0 t \right) \quad (40)$$

$$v_c(t) = \frac{1}{2} [V_s(1 - \cos \omega_0 t) + Z_0 I_{ZVS} \sin \omega_0 t], \quad (41)$$

where $\omega_0 = \frac{1}{\sqrt{LC_{oss}}}$, $Z_0 = \sqrt{\frac{L}{C_{oss}}}$. When diodes D_1 and D_4 conduct, the current of the inductor decreases (the absolute value) linearly. The curves of $i_L(t)$ and $v_c(t)$ are given in Fig. 16.

Compared with the estimation equation of (37), the equations during the resonant interval show more information, which helps to better determine the needed switched ZVS current and dead time. For example, by solving (41) to make v_c equal to V_s , the minimum dead time needed to achieve ZVS turn-ON is

$$t_{\min} = \frac{1}{\omega_0} \arcsin \frac{2kV_s}{k^2 + V_s^2}, \quad (42)$$

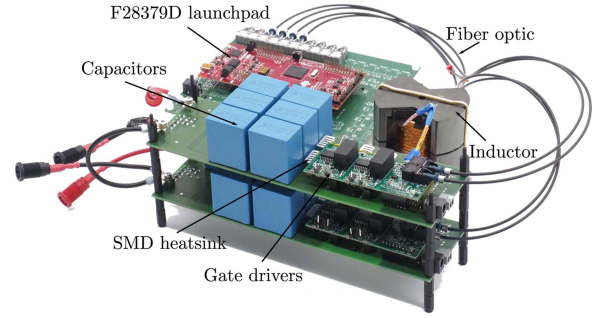


Fig. 17. Four-switch buck+boost converter prototype.

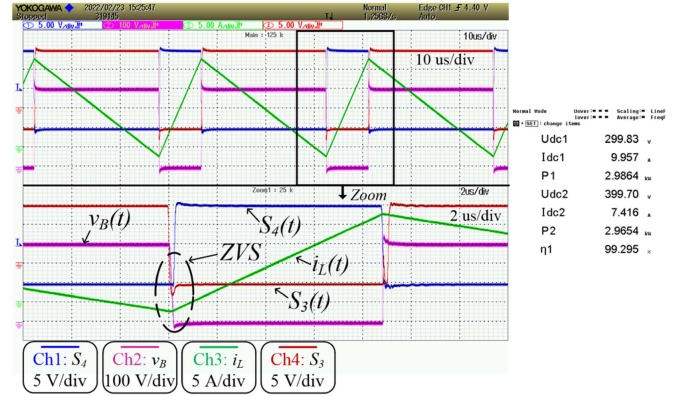


Fig. 18. Boost-type operating mode: measured waveforms and efficiency at $V_1 = 300$ V and $V_2 = 400$ V, $P_o = 3$ kW. $S_4(t)$ is the gate–source voltage of S_4 , $S_3(t)$ is the gate–source voltage of S_3 , $i_L(t)$ is the inductor current, $v_B(t)$ is the voltage potential of point B relative to the bottom-side (or lower potential) dc-bus rail shown in Fig. 1. Efficiency was measured by Yokogawa WT500 power analyzer. Udc1 and Idc1 are the values from input side while Udc2 and Idc2 are the values from the output side.

where $k = I_{ZVS} Z_0$. Substitute (42) back into (40), then the inductor current value returns back to its initial value of $-I_{ZVS}$.

It should be noted that in reality, the value of C_{oss} is nonlinear and voltage-dependent. It is better to find the appropriate current value through some experimental tests. Based on the discussion above, to start the test of the converter for ZVS realization, a switched current of -2 to -3 A and a dead time of 200 to 300 ns is a suitable choice for the designed prototype.

IV. EXPERIMENTAL VERIFICATION

In order to verify the proposed control strategy, a 300–600 V input, 400 V output four-switch buck+boost converter with rated power of 3 kW was designed and constructed. The converter is set to operate with a power from 10% to full rated load and the efficiency will be measured with a Yokogawa WT500 power analyzer.

The converter prototype is shown in Fig. 17. Three SMD SiC MOSFETS of G3R75MT12J were connected in parallel to form a single switch to increase the current rating capability.

After hardware commissioning, the negative ZVS switched current was selected to be -2.5 A and the dead time was set to 200 ns. The calculated power loss distributions at the worst

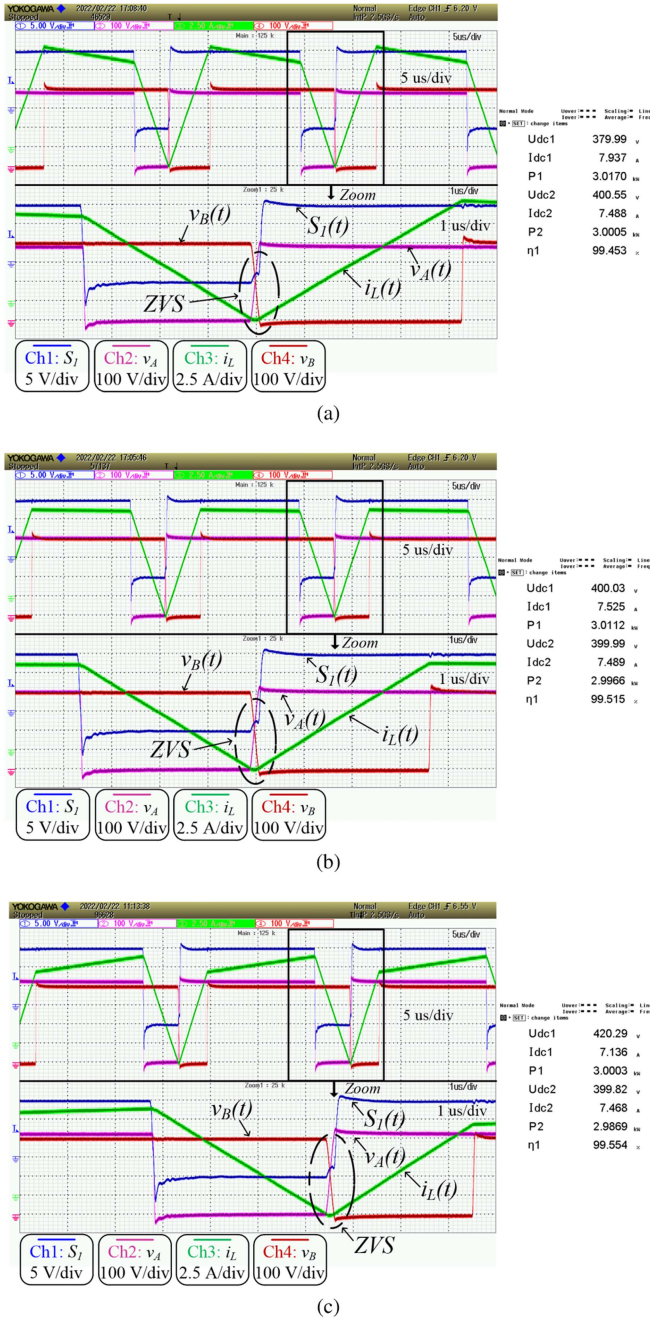


Fig. 19. Buck-boost-type operating mode: measured waveforms and efficiency at $V_1 = 380, 400,$ and 420 V , $P_o = 3\text{ kW}$, $d_1 = 0.8$, $V_2 = 400\text{ V}$. $S_1(t)$ is the gate-source voltage of S_1 , $v_A(t)$ is the voltage potential of point A relative to the bottom-side (or lower potential) dc-bus rail shown in Fig. 1. (a) $V_1 = 380\text{ V}$. (b) $V_1 = 400\text{ V}$. (c) $V_1 = 420\text{ V}$.

case when $V_1 = 300\text{ V}$, $V_2 = 400\text{ V}$, and $P_o = 3\text{ kW}$ are given in Table III.

A. Steady-State Operation

Since there are three operating modes of this buck+boost converter, so, the experimental results at several typical input voltage values of these three modes will be given.

TABLE III
WORST CASE ($V_1 = 300\text{ V}$, $V_2 = 400\text{ V}$) CALCULATED POWER LOSSES DISTRIBUTION AND CONVERTER EFFICIENCY

Total losses	15.63 W
Semiconductor	10.13 W
Winding	2.28 W
Core	3.10 W
Input capacitor	0.06 W
Output capacitor	0.06 W
Efficiency \approx	99.48%

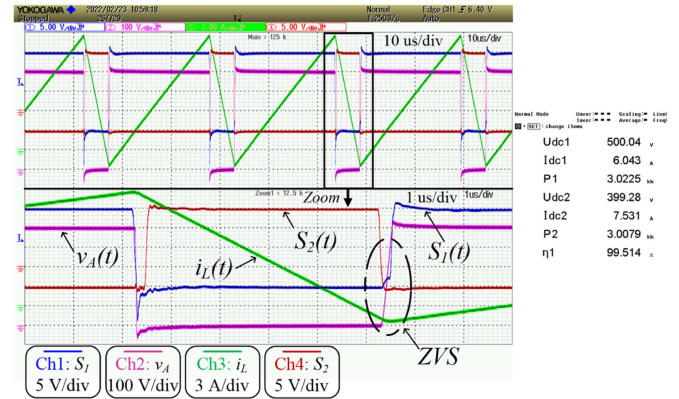


Fig. 20. Buck-type operating mode: measured waveforms and efficiency at $V_1 = 500\text{ V}$ and $V_2 = 400\text{ V}$, $P_o = 3\text{ kW}$. $S_2(t)$ is the gate-source voltage of S_2 .

Fig. 18 shows the experimental results in boost-type mode at 3 kW when V_1 is 300 V and V_2 is 400 V . It can be seen that the MOSFET S_4 turned on at zero voltage. The measured efficiency was 99.30% .

In the buck-boost-type mode, V_1 was tested at three typical voltage values of 380 V , 400 V , and 420 V , respectively, and d_1 was fixed at 0.8 . The measurement results are given in Fig. 19. As it can be seen from the voltages of v_A and v_B at the switching point when i_L is -2.5 A , v_A reached V_1 while v_B dropped to zero when turning on S_1 and S_4 , therefore, the ZVS turn-ON of these two switches was achieved. Since the inductor current at the other two switching points were much larger, therefore, the ZVS turn-ON of the four MOSFETS were all accomplished.

The measured result of the buck-type operating mode when V_1 is 500 V is shown in Fig. 20. It can be seen that v_A has reached V_1 when S_1 was turned on, so, S_1 has achieved ZVS turn-ON and the measured power efficiency was 99.51% .

Efficiency curves at different input and output voltages are shown in Fig. 21. Apart from the performance at 400 V output, the measured efficiency was also given at 360 V output, which covers the battery voltage range of most common commercial EVs. It can be seen that in the power range from 1 to 3 kW , all the measured points show efficiency higher than 99% at 400 V output, i.e., between 99.2% and 99.6% .

By comparing the efficiency curves at different input voltage values, one can find that the efficiency in the buck-boost-type mode drops more evidently due to the ZVS turn-ON loss of a certain switch. For example, Fig. 22 shows the ZVS turn-ON loss of S_3 at 380 W when $V_1 = 420\text{ V}$ and $V_2 = 400\text{ V}$, which

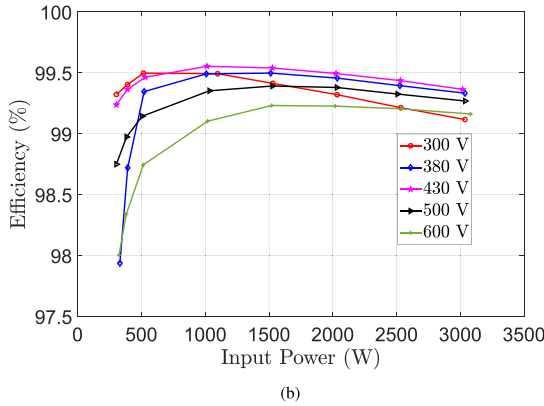
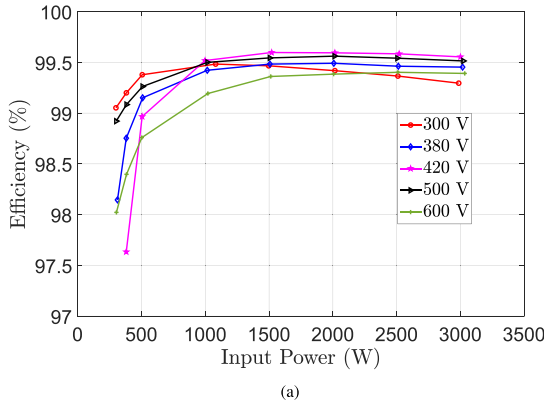


Fig. 21. Measured power efficiency curves at different input and output voltages. (a) $V_2 = 400$ V. (b) $V_2 = 360$ V.

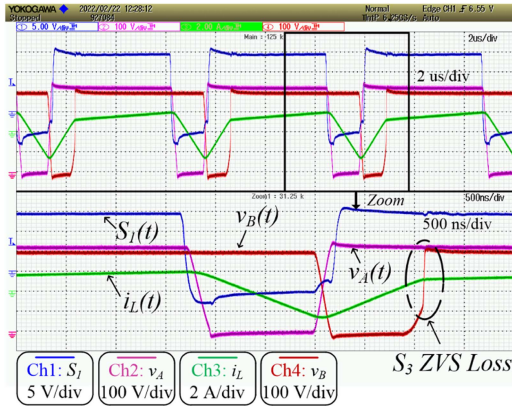


Fig. 22. ZVS turn-ON loss of S_3 , $V_1 = 420$ V, $V_2 = 400$ V, and $P_o = 380$ W.

can be seen from its sudden drain-source voltage change. As mentioned in Section II, to decrease the duty cycle of S_1 is a possible solution to guarantee ZVS even in the light load condition. However, further optimization through dynamic duty cycle control is out of this article’s scope.

The power density of this converter is 4.86 kW/L with the volume information of each part shown in Table IV.

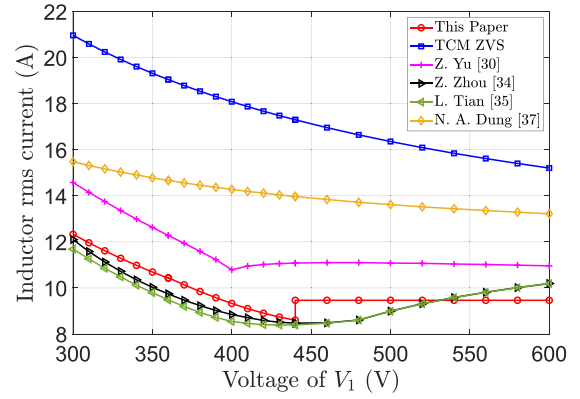


Fig. 23. Inductor current rms value comparison under different control schemes. $V_2 = 400$ V, $P_o = 3$ kW, absolute value of ZVS current is 2.5 A.

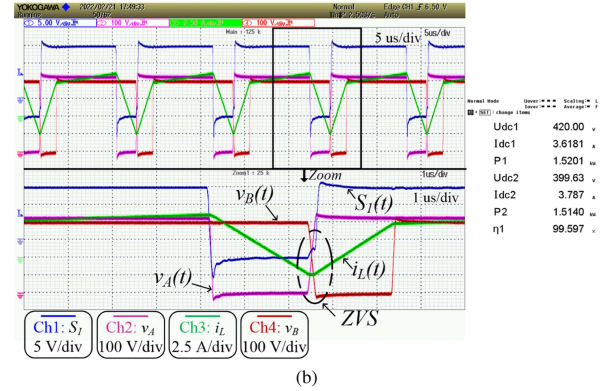
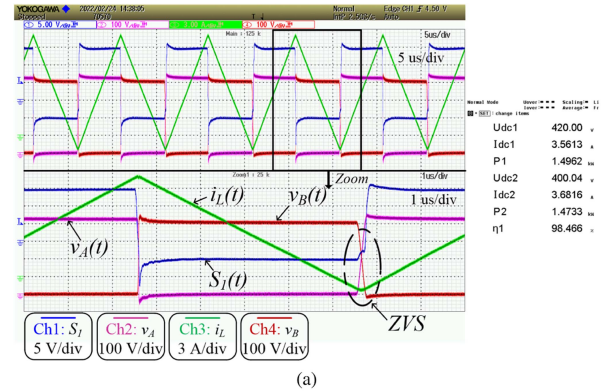


Fig. 24. Measured waveforms and efficiency at $V_1 = 420$ V, $V_2 = 400$ V, $P_o = 1500$ W. An efficiency improvement of 1.13% can be seen. (a) TCM-ZVS buck-boost-type operation. (b) ZVS scheme adopted in this article.

TABLE IV
VOLUME OF EACH PART OF THE CONVERTER

	Inductor	Capacitors	Heatsink (With MOSFETs)	Driver
Volume (L)	0.18	0.325	0.027	0.085
Volume Percent (%)	29.2	52.7	4.4	13.8

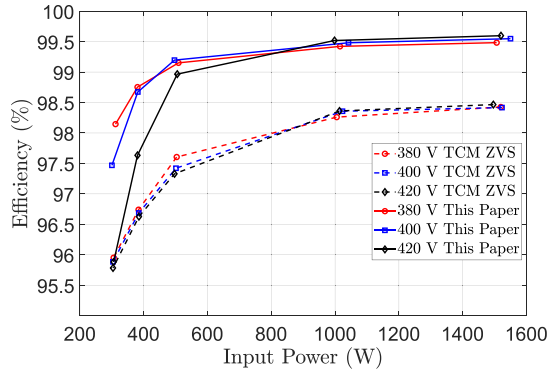


Fig. 25. Comparison of measured efficiency results. The dotted lines represent the TCM buck-boost-type mode operation while the solid lines represent efficiency measured with the scheme adopted in this article.

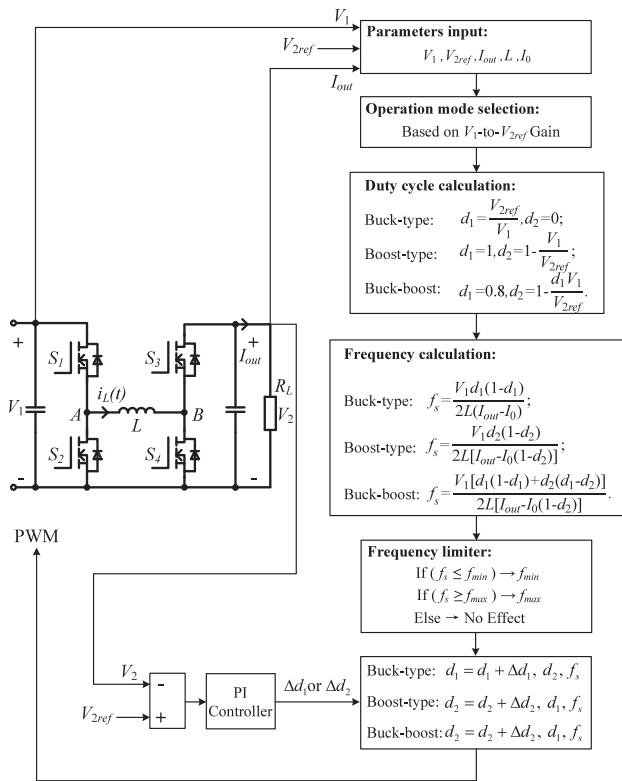
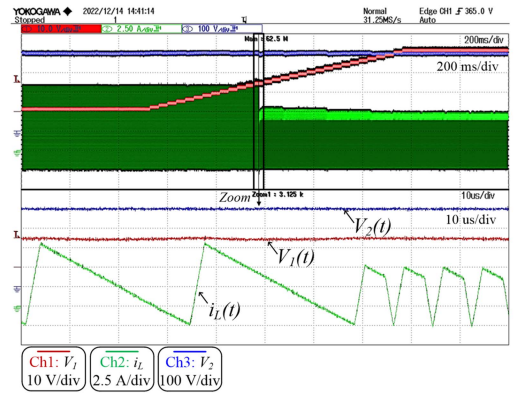


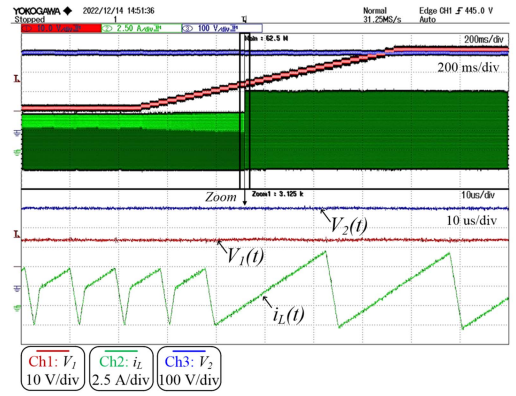
Fig. 26. Closed-loop control algorithm implemented during mode transition test, I_0 is the switched ZVS current, which is -2.5 A.

B. Benchmark With Different ZVS Control Schemes

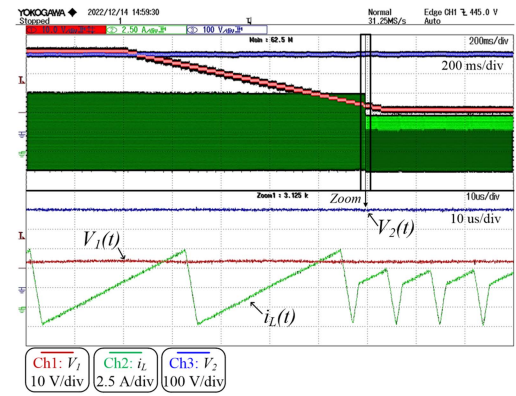
Fig. 23 compares the obtained inductor current rms value under different control schemes at full load. The TCM ZVS control is the modulation method that the switches S_1 and S_4 turn on/off simultaneously. For both methods in [34] and [37], the inductor current rms value is calculated with an inductance of $100 \mu\text{H}$ and frequency of 50 kHz. For the method in [35], the inductance is $100 \mu\text{H}$ and the frequency varies between 42.5 kHz and 50 kHz. As it can be seen, the inductor current rms value proposed in [34] and [35] showed a smaller value in a wide range, however, Zhou et al. [34] adopt a fixed-frequency four-segment inductor current modulation while a combination



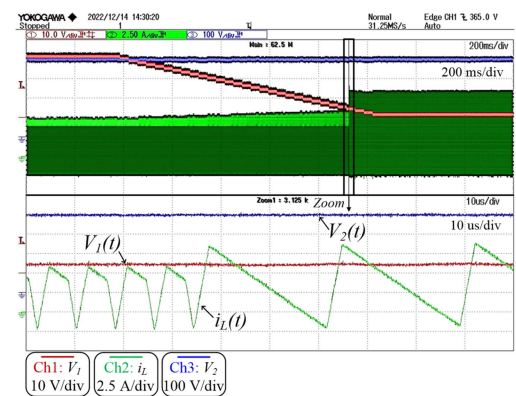
(a)



(b)



(c)



(d)

Fig. 27. Mode transition tested at 1 kW and 400 V output. (a) $V_1 = 350 - 380$ V. (b) $V_1 = 430 - 460$ V. (c) $V_1 = 460 - 430$ V. (d) $V_1 = 380 - 350$ V.

control of fixed- and variable-frequency modulation is adopted in [35], compared with the method in this article, the modulation techniques are different. Besides, the selection of the optimal switching times in [34] and [35] is more complicated.

Apart from the comparison of the current rms value under different control schemes, tests were also carried out between the TCM ZVS control and the proposed control in the buck-boost-type region. Due to the high peak inductor current in the TCM-ZVS operation, the power efficiency between 1500 W and 300 W was measured and compared. Fig. 24 shows the measured results at 1500 W. As it can be seen, the power efficiency was improved by 1.13% with the ZVS scheme adopted in this article, and the losses were reduced from 22.9 to 6.1 W. The measured efficiency curves of these two schemes are presented in Fig. 25.

C. Mode Transition Operation

The mode transition is implemented based on the method given in Fig. 26, $V_{2\text{ref}}$ is the reference value for the output voltage. In order to prevent the switching frequency from swinging frequently at the boundaries between the operational modes (cf. Fig. 13), a hysteresis of ΔV was applied to avoid this issue.

The mode transition was tested at 1 kW and 400 V output. Fig. 27 shows the mode transition results when the input voltage increases or decreases to cover all the possible cases in this article's study. For example, in Fig. 27(a), it shows the transition from boost-type mode to buck-boost-type mode when V_1 increases from 350 to 380 V. As it can be seen, there is no much visible oscillations of the inductor current during mode transitions.

V. CONCLUSION

In this article, the ZVS realization in a four-switch buck+boost converter was analyzed and presented comprehensively in three mode operation by variable frequency technique. TCM-ZVS buck-type or boost-type modulation strategy was adopted when the input voltage is in the higher or lower voltage range. In the buck-boost-type mode when the input-to-output voltage gain is close to unit, three-segment inductor current modulation is found to be the most suitable modulation method. A 300–600 V input, 400 V output, 3 kW laboratory prototype was built to prove and verify the proposed concepts. The converter was tested in a wide power range from 10% to full rated load. The measured efficiency was always higher than 99%, i.e., between 99.2% and 99.6%, from 1 to 3 kW for all the considered input voltages. Mode transition test was also carried out to show the feasibility of the proposed modulation strategy. The power density of this converter is 4.86 kW/L. The dynamic duty cycle control can be a future study to further improve the efficiency in the transition mode at light load.

APPENDIX A

RMS VALUE OF A GENERAL POLYLINE FUNCTION

Fig. 28 shows a general polyline function with values of y_1 at x_1 , y_2 at x_2 , etc.

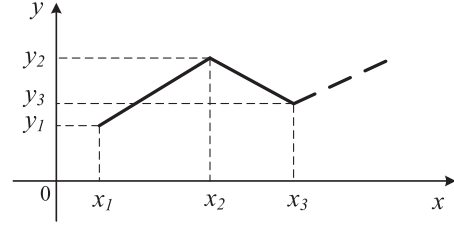


Fig. 28. General polyline function.

Based on the definition of rms value of a function, it is

$$F_{\text{rms}} = \sqrt{\frac{1}{T} \int_0^T f^2(x) dx} = \sqrt{\frac{1}{T} \left[\int_{x_1}^{x_2} f^2(x) dx + \int_{x_2}^{x_3} f^2(x) dx + \dots \right]}. \quad (\text{A1})$$

In (A1), T is the period of the function. The function expression from x_1 to x_2 can be written as $f(x) = kx + b$ with $k = \frac{y_2 - y_1}{x_2 - x_1}$ and $b = y_1 - kx_1$. Substitute this equation into (A1), after simplification, (A2) is derived as

$$\begin{aligned} \sqrt{\frac{1}{T} \int_{x_1}^{x_2} f^2(x) dx} &= \sqrt{\frac{1}{T} \int_{x_1}^{x_2} (kx + b)^2 dx} \\ &= \sqrt{\frac{x_2 - x_1}{T} \frac{y_1^2 + y_2^2 + y_1 y_2}{3}}. \end{aligned} \quad (\text{A2})$$

Therefore, the rms value of a general polyline function can be expressed as

$$F_{\text{rms}} = \sqrt{\frac{x_2 - x_1}{T} \frac{y_1^2 + y_2^2 + y_1 y_2}{3} + \frac{x_3 - x_2}{T} \frac{y_2^2 + y_3^2 + y_2 y_3}{3} + \dots}. \quad (\text{A3})$$

REFERENCES

- [1] M. Yilmaz and P. T. Krein, "Review of battery charger topologies, charging power levels, and infrastructure for plug-in electric and hybrid vehicles," *IEEE Trans. Power Electron.*, vol. 28, no. 5, pp. 2151–2169, May 2013.
- [2] M. Stecca, L. R. Elizondo, T. B. Soeiro, P. Bauer, and P. Palensky, "A comprehensive review of the integration of battery energy storage systems into distribution networks," *IEEE Open J. Ind. Electron. Soc.*, vol. 1, pp. 46–65, 2020.
- [3] S. M. Lukic, J. Cao, R. C. Bansal, F. Rodriguez, and A. Emadi, "Energy storage systems for automotive applications," *IEEE Trans. Ind. Electron.*, vol. 55, no. 6, pp. 2258–2267, Jun. 2008.
- [4] H. K. Bai et al., "Charging electric vehicle batteries: Wired and wireless power transfer: Exploring EV charging technologies," *IEEE Power Electron. Mag.*, vol. 9, no. 2, pp. 14–29, Jun. 2022.
- [5] W. Shi et al., "Design of a highly efficient 20-kW inductive power transfer system with improved misalignment performance," *IEEE Trans. Transport. Electrification.*, vol. 8, no. 2, pp. 2384–2399, Jun. 2022.
- [6] J. Garnica, R. A. Chinga, and J. Lin, "Wireless power transmission: From far field to near field," *Proc. IEEE*, vol. 101, no. 6, pp. 1321–1331, Jun. 2013.
- [7] F. Grazian, W. Shi, T. B. Soeiro, J. Dong, and P. Bauer, "Electric vehicle charging based on inductive power transfer employing variable compensation capacitance for optimum load matching," in *Proc. IEEE 46th Annu. Conf. Ind. Electron. Soc.*, 2020, pp. 5262–5267.
- [8] Y. Huang, N. Shinohara, and T. Mitani, "Impedance matching in wireless power transfer," *IEEE Trans. Microw. Theory Techn.*, vol. 65, no. 2, pp. 582–590, Feb. 2017.

- [9] M. Fu, C. Ma, and X. Zhu, "A cascaded boost–buck converter for high-efficiency wireless power transfer systems," *IEEE Trans. Ind. Inform.*, vol. 10, no. 3, pp. 1972–1980, Mar. 2014.
- [10] *Wireless Power Transfer for Light-Duty Plug-in/Electric Vehicles and Alignment Methodology*. Warrendale, PA, USA: SAE Int., 2020.
- [11] L. Tai, M. Lin, J. Wang, and C. Hou, "Synchronous control strategy with input voltage feedforward for a four-switch buck-boost converter used in a variable-speed PMSG energy storage system," *Electronics*, vol. 10, no. 19, 2021, Art. no. 2375.
- [12] F. Caricchi, F. Crescimbeni, and A. Di Napoli, "20 kW water-cooled prototype of a buck-boost bidirectional DC-DC converter topology for electrical vehicle motor drives," in *Proc. IEEE Appl. Power Electron. Conf. Expo.*, 1995, pp. 887–892.
- [13] G. Stahl, M. Rodriguez, and D. Maksimovic, "A high-efficiency bidirectional buck-boost DC-DC converter," in *Proc. IEEE 27th Annu. Appl. Power Electron. Conf. Expo.*, 2012, pp. 1362–1367.
- [14] X. Chen, A. A. Pise, J. Elmes, and I. Batarseh, "Ultra-highly efficient low-power bidirectional cascaded buck-boost converter for portable PV-battery-devices applications," *IEEE Trans. Ind. Appl.*, vol. 55, no. 4, pp. 3989–4000, Jul./Aug. 2019.
- [15] F. Caricchi, F. Crescimbeni, F. Capponi, and L. Solero, "Study of bidirectional buck-boost converter topologies for application in electrical vehicle motor drives," in *Proc. IEEE 13th Annu. Appl. Power Electron. Conf. Expo.*, 1998, pp. 287–293.
- [16] E. Schaltz, P. O. Rasmussen, and A. Khaligh, "Non-inverting buck-boost converter for fuel cell applications," in *Proc. IEEE 34th Annu. Conf. Ind. Electron.*, 2008, pp. 855–860.
- [17] J. Xu, T. B. Soeiro, Y. Wang, F. Gao, H. Tang, and P. Bauer, "A hybrid modulation featuring two-phase clamped discontinuous PWM and zero voltage switching for 99% efficient DC-type EV charger," *IEEE Trans. Veh. Technol.*, vol. 71, no. 2, pp. 1454–1465, Feb. 2022.
- [18] C. Henze, H. Martin, and D. Parsley, "Zero-voltage switching in high frequency power converters using pulse width modulation," in *Proc. IEEE 3rd Annu. Appl. Power Electron. Conf. Expo.*, 1988, pp. 33–40.
- [19] O. Knecht, D. Bortis, and J. W. Kolar, "Comparative evaluation of a triangular current mode (TCM) and clamp-switch TCM DC-DC boost converter," in *Proc. IEEE Energy Convers. Congr. Expo.*, 2016, pp. 1–8.
- [20] J. Zhang, J.-S. Lai, R.-Y. Kim, and W. Yu, "High-power density design of a soft-switching high-power bidirectional DC–DC converter," *IEEE Trans. Power Electron.*, vol. 22, no. 4, pp. 1145–1153, Jul. 2007.
- [21] K. Kruse, M. Elbo, and Z. Zhang, "GaN-based high efficiency bidirectional DC-DC converter with 10 MHz switching frequency," in *Proc. IEEE Appl. Power Electron. Conf. Expo.*, 2017, pp. 273–278.
- [22] X. Ren, X. Ruan, H. Qian, M. Li, and Q. Chen, "Three-mode dual-frequency two-edge modulation scheme for four-switch buck–boost converter," *IEEE Trans. Power Electron.*, vol. 24, no. 2, pp. 499–509, Feb. 2009.
- [23] Z. Yu, H. Kapels, and K. F. Hoffmann, "High efficiency bidirectional DC-DC converter with wide input and output voltage ranges for battery systems," in *Proc. PCIM Eur. Int. Exhib. Conf. Power Electron. Intell. Motion Renewable Energy Energy Manage.*, 2015, pp. 1–8.
- [24] H. Kobayashi, "Circuit of high efficient buck-boost switching regulator and control method thereof," U.S. Patent App. 12/928 876, Jun. 14, 2012.
- [25] D.-H. Kim and B.-K. Lee, "An enhanced control algorithm for improving the light-load efficiency of noninverting synchronous buck–boost converters," *IEEE Trans. Power Electron.*, vol. 31, no. 5, pp. 3395–3399, May 2016.
- [26] J. Liu, K. L. Wong, S. Allen, and J. Mookken, *Performance Evaluations of Hard-Switching Interleaved DC/DC Boost Converter With New Generation Silicon Carbide Mosfets*. Goleta, CA, USA: Cree Inc., 2013, pp. 1–6.
- [27] Z. Zhang et al., "High-efficiency silicon carbide-based buck-boost converter in an energy storage system: Minimizing complexity and maximizing efficiency," *IEEE Ind. Appl. Mag.*, vol. 27, no. 3, pp. 51–62, May/Jun. 2021.
- [28] S. Waffler and J. W. Kolar, "A novel low-loss modulation strategy for high-power bidirectional buck + boost converters," *IEEE Trans. Power Electron.*, vol. 24, no. 6, pp. 1589–1599, Jun. 2009.
- [29] A. J. Hanson, R. S. Yang, S. Lim, and D. J. Perreault, "A soft-switched high frequency converter for wide voltage and power ranges," in *Proc. IEEE Int. Telecommun. Energy Conf.*, 2016, pp. 1–8.
- [30] Z. Yu, H. Kapels, and K. F. Hoffmann, "Extreme high efficiency non-inverting buck-boost converter for energy storage systems," in *Proc. Int. Exhib. Conf. Power Electron. Intell. Motion Renewable Energy Energy Manage.*, 2016, pp. 1–8.
- [31] Z. Yu, H. Kapels, and K. F. Hoffmann, "A novel control concept for high-efficiency power conversion with the bidirectional non-inverting buck-boost converter," in *Proc. IEEE 18th Eur. Conf. Power Electron. Appl.*, 2016, pp. 1–10.
- [32] T. Fang, Y. Wang, H. Zhang, Y. Zhang, S. Sheng, and J. Lan, "An improved three-mode variable frequency control strategy based on four-switch buck-boost converter," *Trans. China Electrotechnical Soc.*, vol. 36, no. 21, pp. 4544–4557, 2021.
- [33] P. Vinciarelli, "Buck-boost DC-DC switching power conversion," U.S. Patent 6 788 033, Sep. 2004.
- [34] Z. Zhou, H. Li, and X. Wu, "A constant frequency ZVS control system for the four-switch buck–boost DC–DC converter with reduced inductor current," *IEEE Trans. Power Electron.*, vol. 34, no. 7, pp. 5996–6003, Jul. 2019.
- [35] L. Tian, X. Wu, C. Jiang, and J. Yang, "A simplified real-time digital control scheme for ZVS four-switch buck-boost with low inductor current," *IEEE Trans. Ind. Electron.*, vol. 69, no. 8, pp. 7920–7929, Aug. 2022.
- [36] Q. Liu, Q. Qian, M. Zheng, S. Xu, W. Sun, and T. Wang, "An improved quadrangle control method for four-switch buck-boost converter with reduced loss and decoupling strategy," *IEEE Trans. Power Electron.*, vol. 36, no. 9, pp. 10827–10841, Sep. 2021.
- [37] N. A. Dung, P. P. Hieu, H.-J. Chiu, Y.-C. Hsieh, and J.-Y. Lin, "A DSP based digital control strategy for ZVS bidirectional buck boost converter," in *Proc. 3rd Int. Conf. Intell. Green Building Smart Grid*, 2018, pp. 1–4.
- [38] K. Xia, Z. Li, Y. Qin, Y. Yuan, and Q. Yuan, "Minimising peak current in boundary conduction mode for the four-switch buck–boost dc/dc converter with soft switching," *IET Power Electron.*, vol. 12, no. 4, pp. 944–954, 2019.
- [39] Z. Zhang, F. Wang, D. J. Costinett, L. M. Tolbert, B. J. Blalock, and H. Lu, "Dead-time optimization of sic devices for voltage source converter," in *Proc. IEEE Appl. Power Electron. Conf. Expo.*, 2015, pp. 1145–1152.
- [40] G. Yu, T. B. Soeiro, J. Dong, and P. Bauer, "Study of back-end DC/DC converter for 3.7 kW wireless charging system according to SAE J2954," in *Proc. IEEE 15th Int. Conf. Compat. Power Electron. Power Eng.*, 2021, pp. 1–8.
- [41] M. R. Rogina, A. Rodriguez, A. Vazquez, and D. G. Lamar, "Improving the efficiency of SiC-based synchronous boost converter under variable switching frequency TCM and different input/output voltage ratios," *IEEE Trans. Ind. Appl.*, vol. 55, no. 6, pp. 7757–7764, Jun. 2019.



Guangyao Yu (Student Member, IEEE) was born in Haiyan, Zhejiang, China. He received the bachelor's degree in electrical engineering and automation in 2015 from Zhejiang University, Hangzhou, China, and the master's degree (with cum laude) in electrical engineering in 2020 from the Delft University of Technology (TU Delft), Delft, The Netherlands, where he is currently working toward the Ph.D. degree in electrical engineering with DCES Group (dc systems, energy conversion, and storage).

From 2016 to 2018, he was with Solax Power Company, Ltd., Hangzhou, China, where he was an Electrical Engineer. His research interests include modulation study of power electronic converters and its application in wireless power transfer.



Jianning Dong (Senior Member, IEEE) received the B.S. and Ph.D. degrees in electrical engineering from Southeast University, Nanjing, China, in 2010 and 2015, respectively.

He was a Postdoctoral Researcher with the McMaster Automotive Resource Centre, McMaster University, Hamilton, ON, Canada. Since 2016, he has been an Assistant Professor with the DC System, Energy Conversion and Storage (DCE&S) Group, Delft University of Technology (TU Delft), Delft, The Netherlands. His research interests include electromechanical energy conversion and contactless power transfer.



Thiago Batista Soeiro (Senior Member, IEEE) received the B.Sc. (Hons.) and M.Sc. degrees in electrical engineering from the Federal University of Santa Catarina, Florianopolis, Brazil, in 2004 and 2007, respectively, and the Ph.D. degree from the Swiss Federal Institute of Technology, Zurich, Switzerland, in 2012.

During the Master and Ph.D. studies, he was a Visiting Scholar with the Power Electronics and Energy Research Group, Concordia University, Montreal, QC, Canada, and with the Center for Power Electronics Systems, Blacksburg, VA, USA, respectively. From 2012 to 2013, he was a Researcher with the Power Electronics Institute, Federal University of Santa Catarina. From October 2013 to April 2018, he was with the Corporate Research Center, ABB Switzerland Ltd., Baden-Dattwil, Switzerland, where he was a Senior Scientist. From May 2018 to January 2022, he was with the DC Systems, Energy Conversion and Storage Group, Delft University of Technology, Delft, The Netherlands, where he was an Associate Professor. From January to October 2022, he was with the Power Management and Distribution Section (TEC-EPM) for the European Space Research and Technology Centre, Noordwijk, The Netherlands. Since October 2022, he has been a Full Professor for Power Electronics with the Power Electronics and EMC group of the University of Twente, Enschede, The Netherlands. His research interests include advanced high power converters and dc system integration.

Dr. Soeiro was a recipient of the 2013 IEEE Industrial Electronics Society Best Conference Paper Award and the Best Paper Awards in the following IEEE conferences: International Conference on Power Electronics (ECCE Asia 2011), the International Conference on Industrial Technology (ICIT 2013), the Conference on Power Electronics and Applications EPE'15 (ECCE Europe 2015), and the International Conference on Power Electronics and Motion Control 2020 and 2022 (PEMC 2020 and 2022).



Gangwei Zhu (Student Member, IEEE) was born in Hunan, China, in 1997. He received the B.S. degree in electrical engineering from Central South University, Changsha, China, in 2018 and the M.S. degree in electrical engineering from Shanghai Jiao Tong University, Shanghai, China, in 2021. He is currently working toward the Ph.D. degree in electrical engineering with DCES Group (dc systems, energy conversion, and storage) of Delft University of Technology, Delft, The Netherlands.

His research interests include advanced control and modulation for wireless power transfer.



Yu Yao (Student Member, IEEE) received the B.S. and Ph.D. degrees in electrical engineering from Southeast University, Nanjing, China, in 2016 and 2022, respectively.

After that, he joined the School of Electrical Engineering, Southeast University, as an Assistant Professor. His main research interests include the design of the power inverter, the current regulator design, the position sensorless drive for the high-speed PMSM, and the drive system with *LCL* output filter.



Pavol Bauer (Senior Member, IEEE) received the master's degree in electrical engineering from the Technical University of Kosice, Kosice, Slovakia, in 1985 and the Ph.D. degree in power electronics from the Delft University of Technology, Delft, The Netherlands, in 1995.

From 2002 to 2003, he was with KEMA (DNV GL), Arnhem, The Netherlands, on different projects related to power electronics applications in power systems. He is currently a Full Professor with the Department of Electrical Sustainable Energy, Delft

University of Technology, and the Head of DC Systems, Energy Conversion, and Storage Group. He is also a Professor with the Brno University of Technology, Brno, Czech Republic, and an Honorary Professor with the Politehnica University Timisoara, Timisoara, Romania. He has authored or coauthored more than 120 journal articles and 500 conference papers in his field. He is an author or coauthor of eight books, holds seven international patents, and organized several tutorials at international conferences. He has worked on many projects for the industry concerning wind and wave energy, power electronic applications for power systems, such as Smarttrafo; HVdc systems, projects for smart cities such as photovoltaic (PV) charging of electric vehicles, PV and storage integration, contactless charging; and he participated in several Leonardo da Vinci and H2020, and Electric Mobility Europe EU projects as a Project Partner (ELINA, INETELE, E-Pragmatic, Micact, Trolley 2.0, OSCD, P2P, and Progressus) and a Coordinator (PEMCWebLab.com-Edipe, SustEner, Eranet DCMICRO).

Dr. Bauer is the Former Chairman of Benelux IEEE Joint Industry Applications Society, Power Electronics and Power Engineering Society Chapter, the Chairman of the Power Electronics and Motion Control Council, a Member of the Executive Committee of European Power Electronics Association, and also a Member of the International Steering Committee at numerous conferences.